

LAMINAR FLOW CONTROL OF A HIGH-SPEED BOUNDARY LAYER BY LOCALIZED WALL HEATING OR COOLING

Fedorov A.V.*, **Soudakov V.G.***, **Egorov I.V.***,
Sidorenko A.A.**, **Gromyko Y.***, **Bountin D.****
***TsAGI, Russia, **ITAM SB RAS and NSU, Russia**

Abstract

A localized heating or cooling effect on stability and transition of the boundary layer flow on a sharp cone at zero angle of attack and free-stream Mach number 6 is analyzed. Experiments were carried out in the Transit-M wind tunnel of Institute of Theoretical and Applied Mechanics (Novosibirsk, Russia) for different heating/cooling intensities and free-stream Reynolds numbers. The mean flows with localized heating/cooling are calculated using axisymmetric Navier-Stokes equations. These solutions are used for the spatial linear stability analysis to estimate the transition onset points using the e^N method. Direct numerical simulations of 2D-disturbances propagating in the boundary layer through the cooled/heated region are performed. The results of stability analysis and numerical simulations are compared with experiments.

1 Introduction

Prediction of laminar-turbulent transition is important for aerothermal design of high-speed vehicles. The surface of such vehicles may have elements of different heat conductivity and/or emissivity. Junctions between these elements lead to jumps of the heat-transfer boundary conditions. These thermal non-uniformities may significantly affect the boundary-layer mean flow, excitation and evolution of unstable modes and, ultimately, the transition locus.

Localized surface heating or cooling can be considered as a technique for laminar flow control. This method was used to suppress the first mode disturbances (Tollmien-Schlichting

waves) [1-2] by local heating in the subsonic boundary layer.

In the present work, we consider a localized heating or cooling on a sharp cone at zero angle of attack at the free-stream Mach number 6. Experimental investigations are performed in the Tranzit-M wind tunnel of Institute of Theoretical and Applied Mechanics (ITAM) of SB RAS (Novosibirsk, Russia). Different intensities and Reynolds numbers are considered. Experimental results are compared with numerical simulations. In these simulations, the steady-state laminar flow solutions are calculated using the Navier-Stokes equations. These solutions provide the mean flow for further calculations of the spatial growth rates and amplification factors for unstable disturbances using LST. The stability data are used to estimate the transition onset points with the help of the e^N method. Experimental and LST results are compared with two-dimensional direct numerical simulations (DNS) of 2D disturbances propagating in the boundary layer through the cooled/heated region.

2 Experimental studies

The ITAM Tranzit-M wind tunnel is a short-time aerodynamic facility with the Mach number range $M=4-8$. Its scheme is shown in Fig. 1. Air is initially accumulated in the first prechamber and volumes of the ohmic heaters, where after heating it acquires high temperature and pressure. After opening of the high-speed valve, the gas is throttled into the second prechamber and then it runs to the test section through the contoured nozzle. The wind tunnel

runtime is limited by the vacuum tank volume. It is approximately equals 110-200 ms for the $M=6$ regime. The wind-tunnel prechambers are equipped by pressure and temperature sensors. The exit diameter of the contoured nozzle is 300 mm.

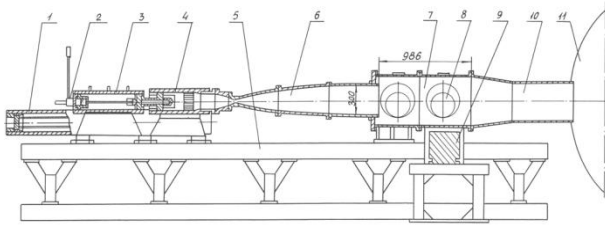


Fig. 1. Wind tunnel "Tranzit-M" (1 - ohmic heater, 2 - high-speed valve, 3 - first prechamber, 4 - second prechamber, 5 - frame, 6 - contoured nozzle, 7 - test section, 8 - optical windows, 9- isolated model base, 10 - diffuser, 11 - vacuum tank).

The experiments were carried out at $M = 5.9$, stagnation temperature $T_0^* = 370 - 410 K$ and the stagnation pressure $p_0^* = 2 - 20 bar$. Hereinafter, asterisks denote dimensional quantities. The free-stream unit Reynolds number has varied in the range of $Re_1 = (4-24) \times 10^6 m^{-1}$. The data are gathered in the time window Δt^* where the p_0^* and T_0^* variations do not exceed 5%. Depending on the initial flow parameters, Δt^* is varied from 90 to 200 ms. The pressure and temperature data readings were averaged over Δt^* to obtain p_0^* and T_0^* for further analysis.

The experimental model is a 7° half-angle cone with a sharp nose (Fig. 2). The model is assembled from four sections including an interchangeable cooler and heater sections. The cooler is made from copper. Its temperature is controlled using liquid nitrogen. The heater has the same cowl and a ceramic insert with ohmic heater inside. The boundaries of heated/cooled region are $x_{S1}^* = 126.2 mm$ and $x_{S1}^* = 203.6 mm$ ($\Delta x_S^* = 77.4 mm$ is the length of the heating/cooling source). The maximum/minimum temperature is achieved for 120÷200 seconds. The main part of the model body is made from PEEK to prevent from the heat diffusion.

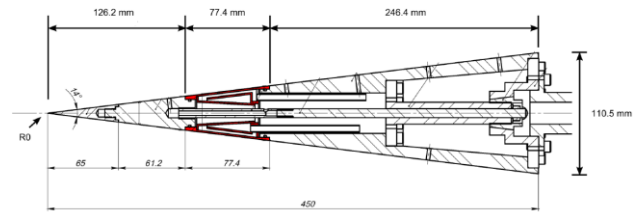


Fig. 2. The 7-degree sharp cone model, dimensions are in mm.

Initially the cone model has the room temperature and the wall temperature distribution is uniform ($T_w^* = 292 K$). After vacuumization of the test chamber the desired temperature T_h^* of the cooled/heated region is achieved and the flow is started as soon as possible after that. The experiments were performed for the free-stream unit Reynolds number from $4.2 \times 10^6 m^{-1}$ to $20 \times 10^6 m^{-1}$, and each run was repeated twice. The five wall-temperature cases were investigated: the baseline flow without heating or cooling, the strong cooling (temperature of the cold region is approximately $T_h^* = 90 K$), the weak cooling ($T_h^* = 120 K$), the weak heating ($T_h^* = 380 K$), and the strong heating ($T_h^* = 440 K$).

The Schlieren images of the flow over the heated and cooled surface regions are shown in Figures 3 and 4 respectively. In these experiments, the knife orientation was horizontal so one can see the corresponding density gradients. The shock wave is followed by the expansion waves in the case of heating. The flow pattern is opposite in the case of cooling.

Turbulent spots were detected in the Schlieren images as zones of the boundary layer inflation. The locations of the inflation beginning were determined for each frame. They are shown in Figure 5. The lines represent the filtered data to reveal a general trend. The running average filter was used with the window of 150 samples. It is seen that the heating shifts the transition onset upstream while the cooling shifts it downstream.

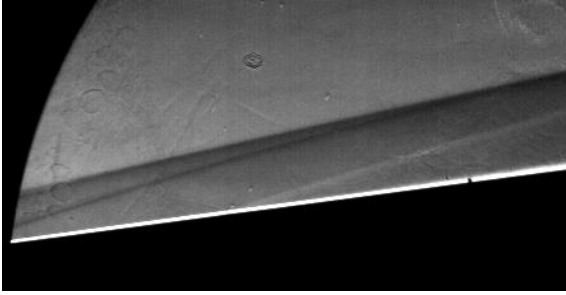


Fig. 3. Schlieren visualization of the flow near the heater with $T_h^* = 440 K$.

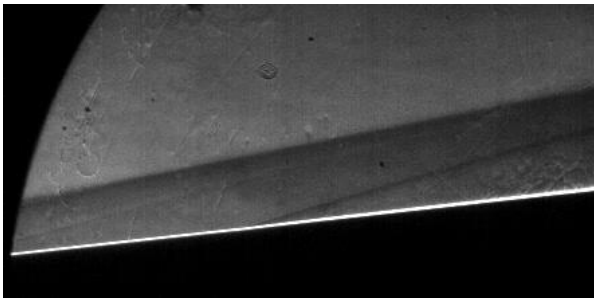


Fig. 4. Schlieren visualization of the flow near the cooler with $T_h^* = 90 K$.

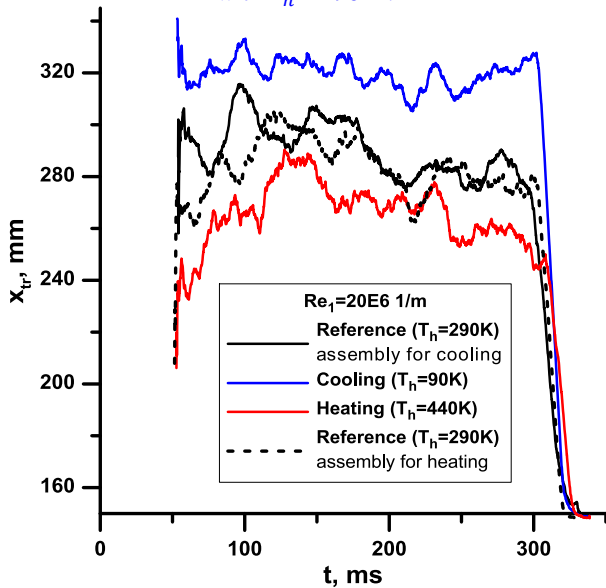


Fig. 5. Transition onset evaluated from the Schlieren images; black lines – baseline case, blue line – strong cooling, red line – strong heating.

The intermittency levels based on the Schlieren visualization are shown in Figure 6. Note that the intermittency is defined as a ratio of the number of frames where the transition was detected upstream from the observation point to the total number of frames. It is seen that the surface cooling effectively delays transition. The heating produces an opposite effect which is less pronounced.

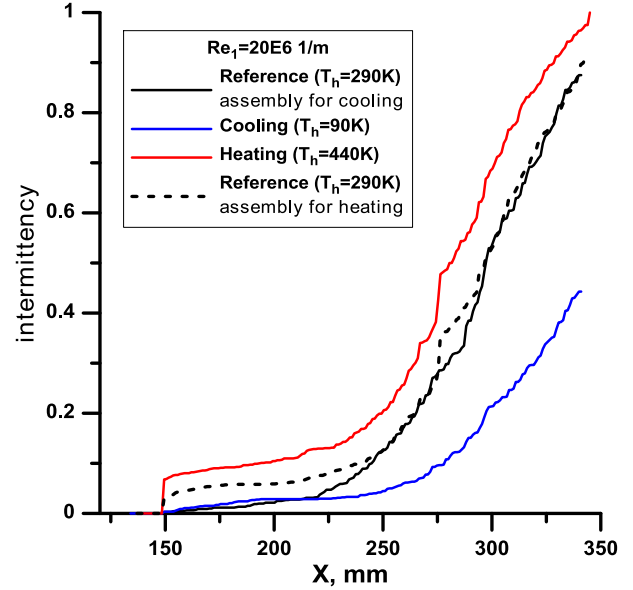


Fig. 6. Intermittency in the transitional boundary layer; black lines – baseline case, blue line – strong cooling, red line – strong heating.

The heat flux distributions were measured at various Re_1 and temperature ratios T_h^*/T_r^* of the cooled/heated region (where T_r^* is the recovery temperature). These distributions are shown in Figure 7. The Stanton number is calculated as $St = Q^*/(Re_{e1}\mu_e^*C_p^*(T_0^* - T_w^*))$, where Q^* is the measured heat flux.

As shown in Figure 7 apparently, the heating or cooling affects the heat transfer to the surface downstream from the active element. The heat flux downstream of the cooler (or heater) is lower (or higher) than in the baseline case.

It is commonly accepted that the heat flux increases in the transitional boundary layer, and the maximum heat flux (or Stanton number) is associated with the end of transition. At $Re_1 = 8.6 \times 10^6 \text{ m}^{-1}$ (Figure 7a), this maximum is observed in the heating case only. As the unit Reynolds number increases, transition moves upstream and the St maximum is clearly observed for the all cases (e.g., Figure 7c). Figures 7a-7c show that the surface cooling shifts the transition location downstream and the magnitude of this shift depends on the temperature ratio T_h^*/T_r^* of the cooled region. The heating shifts the transition locus upstream and this effect is less pronounced.

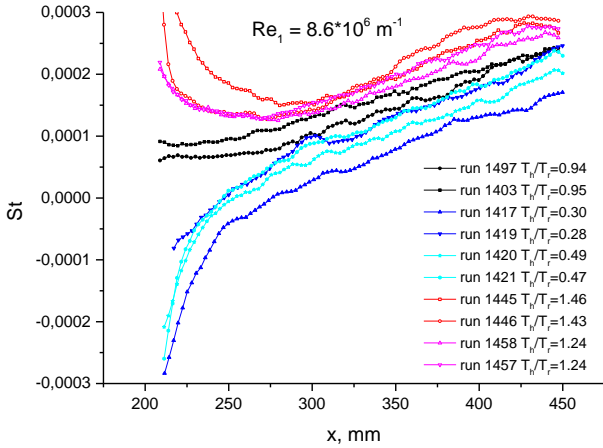


Fig. 7a.

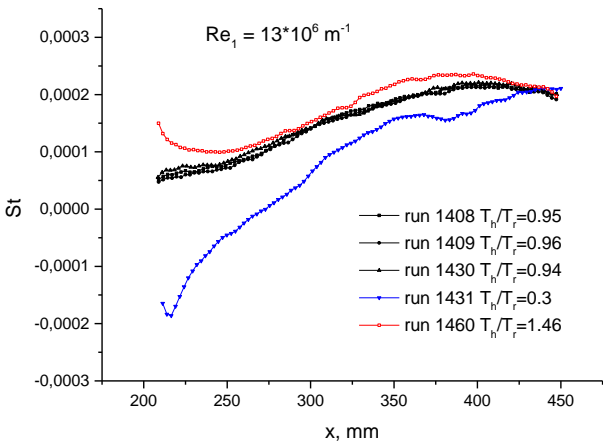


Fig. 7b.

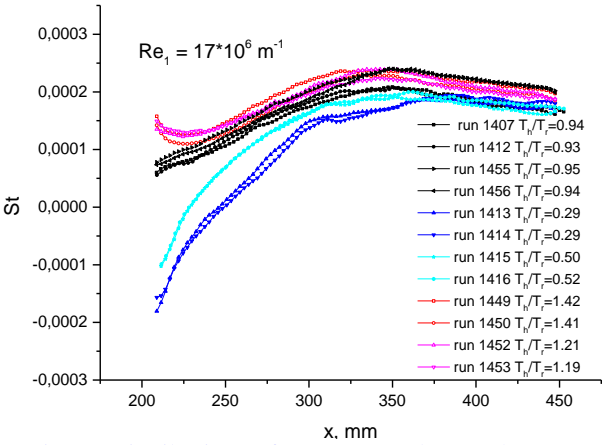


Fig.7c. Distributions of Stanton number on the cone surface for various unit Reynolds numbers and different T_h^*/T_r^* .

3 Numerical solution for the mean flow

Viscous axisymmetric unsteady compressible flows are described by the Navier-Stokes equations. Numerical simulations are carried out for a sharp cone of 7° half angle. The flow variables are made nondimensional using

the free-stream parameters denoted by the subscript “ ∞ ”: $(u, v) = (u^*, v^*)/U_\infty^*$ are longitudinal and vertical velocity components, $p = p^*/(\rho_\infty^* U_\infty^{*2})$ is pressure, $\rho = \rho^*/\rho_\infty^*$ is density, $T = T^*/T_\infty^*$ is temperature. The nondimensional coordinates are $(x, y) = (x^*, y^*)/L^*$ and time is $t = t^* U_\infty^*/L^*$, where U_∞^* is the free-stream velocity, L^* is the cone length, x^* is measured from the cone tip along the cone axis. The fluid is a perfect gas with the specific heat ratio $\gamma = 1.4$ and Prandtl number $Pr = 0.72$. Calculations are performed for the free-stream Mach number 6 and Reynolds number (based on the free-stream parameters and the cone length) $Re = \rho_\infty^* U_\infty^* L^*/\mu_\infty^*$, where μ_∞^* is free-stream dynamic viscosity. The viscosity-temperature dependence is approximated by the Sutherland law with the Sutherland constant 110.4 K. The flow parameters correspond to the experimental conditions. The computational domain is a rectangle with its bottom side corresponding to the cone surface for the region $0 \leq x \leq 1$. The boundary conditions on the cone surface are the no-slip condition and the constant wall temperature $T_w^* = 292$ K. On the outflow boundary, the unknown dependent variables are extrapolated using the linear approximation. On the inflow and upper boundaries, the conditions correspond to the undisturbed free stream. The upper boundary is located above the cone-induced shock wave.

To simulate heating/cooling source the wall temperature is specified as:

$$T_{cone} = \begin{cases} T_w + 0.5(T_h - T_w)[1 + \tanh(70(x - x_{S1}))], & x \in [0.1, 0.5(x_{S1} + x_{S2})] \\ T_w + 0.5(T_h - T_w)[1 - \tanh(70(x - x_{S2}))], & x \in [0.5(x_{S1} + x_{S2}), 0.5] \\ T_w, & x \text{ other than } [0.1, 0.5] \end{cases}$$

where $x_{S1} = 0.2524$ is the upstream boundary of the heater/cooler and $x_{S2} = 0.4072$ is its downstream boundary. The temperature distribution is smoothed near the boundaries in accord with the experimental measurements of the surface temperature.

The problem is solved numerically using the implicit second-order finite-volume method described in [3]. The two-dimensional (axisymmetric) Navier-Stokes equations are approximated by a shock-capturing scheme that allows for modeling of flow non-uniformities in the temperature jump vicinity. The advection terms are approximated by the third-order WENO scheme to decrease the numerical dissipation. Herein the computational grid has 478×599 nodes. The grid is clustered in the direction normal to the cone surface so that the boundary-layer region contains approximately 50% of nodes. The code algorithm as well as its implementations and validations are discussed in [3].

First, the steady-state solution is calculated to provide the mean flow field for the baseline case without heating or cooling. The pressure field is shown in Figure 8 for $Re_L = 4.51 \times 10^6$. Using this numerical solution we can determine flow parameters on the upper boundary-layer edge (denoted by subscript “e”). In the mid station $x = 0.5$, these parameters are $T_e = 1.225$, $U_e = 0.984$, $M_e = 5.33$, the unit Reynolds number $Re_{e1} = 11 \times 10^6 \text{ m}^{-1}$.

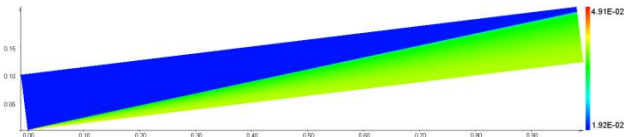


Fig. 8. The mean-flow pressure field past the cone without heating or cooling.

Five different temperature distributions were numerically simulated: baseline flow without heating or cooling, strong cooling, weak cooling, weak heating, strong heating. These cases correspond to experimental conditions of the ITAM Transit-M wind tunnel. The free-stream and surface parameters are given in the table. It should be noted that the temperature difference for the case of strong heating is approximately the same as in the case of weak cooling.

Figure 9 shows the pressure field in the range of $0.22 \leq x \leq 0.46$ for the strong cooling case. Because of the wall temperature drop near the upstream boundary $x_{S1} = 0.2524$, the boundary-layer temperature and its thickness decrease downstream. This causes expansion

waves emanating from the drop vicinity. Near the downstream boundary $x_{S2} = 0.4072$, the wall temperature rise produces an opposite effect causing compression waves.

Name	M_∞	$Re_{\infty L}$ mio	T_∞^* K	T_w^* K	ΔT_h^* K
Baseline	6	4.51	44.24	292	0
Strong cooling	6	4.45	44.94	292	-204.6
Weak cooling	6	4.44	44.61	292	-146.2
Weak heating	6	4.57	43.85	292	85.7
Strong heating	6	4.46	44.70	292	151.7

The same fields are shown in Figure 10 for the heating strip. Now the wall temperature rises near the upstream boundary x_{S1} and drops near the downstream boundary x_{S2} . The compression waves are formed near the first point, while the expansion waves are formed near the second point. The displacement thickness distributions δ^* are shown in figure 11.

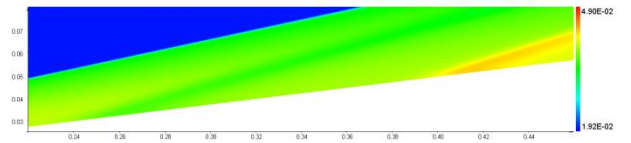


Fig. 9. Pressure fields of the mean flow near the cone surface with the strong cooling strip, $0.22 \leq x \leq 0.46$.

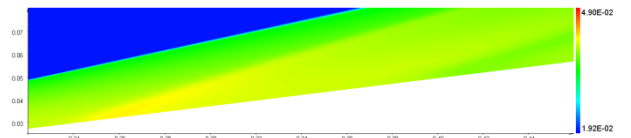


Fig. 10. Pressure fields of the mean flow near the cone surface with the strong heating strip, $0.22 \leq x \leq 0.46$.

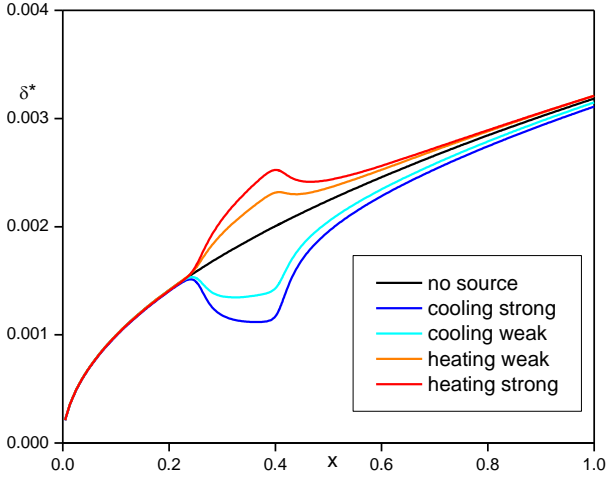


Fig. 11. Boundary-layer displacement thickness for different cases given in the table.

4 Stability analysis

The growth rates and downstream amplifications of convectively unstable disturbances are computed with the help of the in-house linear stability code. This code solves the linear stability equations for compressible boundary-layer flow using a 4th-order Runge-Kutta scheme and a Gram-Schmidt orthonormalization procedure. The eigenvalues of the discrete spectrum are calculated with the help of a shooting/Newton-Raphson procedure. Hereafter we focused on the Mack second mode whose maximal growth rates correspond to 2D waves. In accord with the local-parallel LST, the disturbance is expressed in the wave form $q = \hat{q}(y)\exp[i(\alpha x - \omega t)]$, where ω is real circular frequency and $\alpha(\omega) = \alpha_r + i\alpha_i$ is complex eigenvalue. The downstream growth of instability is characterized by the N-factor

$$N(x, \omega) = \int_{x_0}^x \sigma(x, \omega) dx,$$

where $\sigma = -\alpha_i$ is the spatial growth rate, and the initial point x_0 should be determined from the receptivity problem. The N factors are computed at various fixed dimensional frequencies ω^* . The transition onset point x_{tr} is estimated from the equation $\max_{\omega^*} N(x_{tr}, \omega^*) = N_{tr}$, where N_{tr} is an empirical constant.

We assume that the second-mode waves of all frequencies are effectively excited near the cone tip and the receptivity process is completed by the station $x_0 = 0.1$. It is also assumed that

in this station the initial amplitudes of unstable waves are approximately the same for all frequencies. Then, the N factors and their envelope should be calculated from the fixed initial point $x_0 = 0.1$.

Note that jumps of the wall temperature near the cooling/heating boundaries cause local non-uniformities of the mean flow, where the nonparallel effects seem to be strong. Since the local-parallel stability analysis near these boundaries is not valid, the e^N results presented hereafter should be treated as a first-cut estimate of the cooling/heating effect.

Figures 12-15 shows N-factors at various frequencies, where $N(x)$ are computed from the initial points $x_0 = 0.1$. Upstream from the cooling strip the N-factors are not affected. In the cooling region (Figures 12 and 13), the N-factor envelope is higher than the baseline case. Then, it decreases sharply and rises again. But it is lower in the cooling case than in the baseline case for the downstream relaxation region.

Distributions of N-factors for the weak and strong heating cases are shown in Figures 13 and 14. The N-factor envelope is affected weakly.

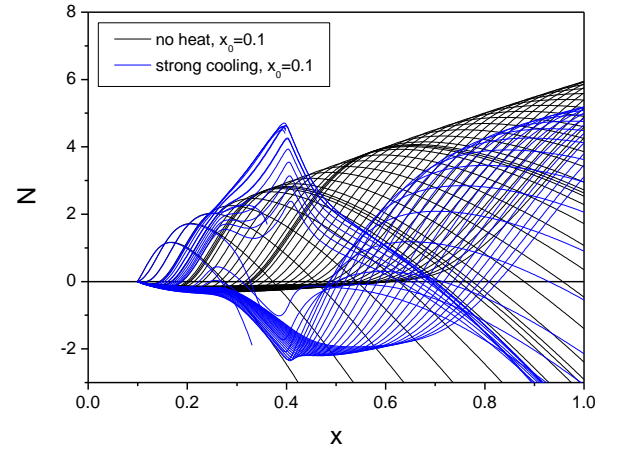


Fig. 12. N-factors for the strong cooling case (blue lines) computed from the fixed point $x_0 = 0.1$ in comparison with baseline case (black lines).

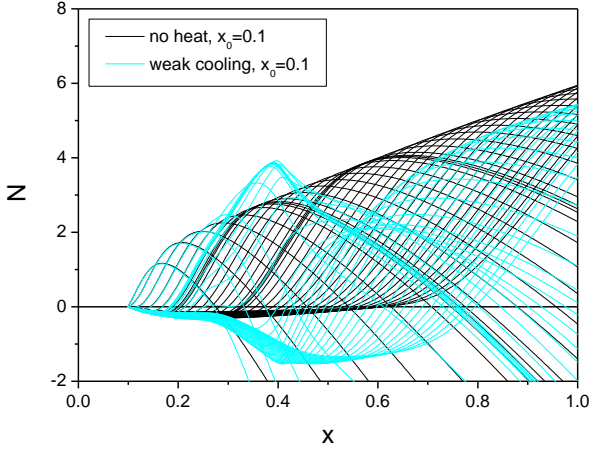


Fig. 13. N-factors for the weak cooling case (cyan lines) computed from the fixed point $x_0 = 0.1$ in comparison with baseline case (black lines).

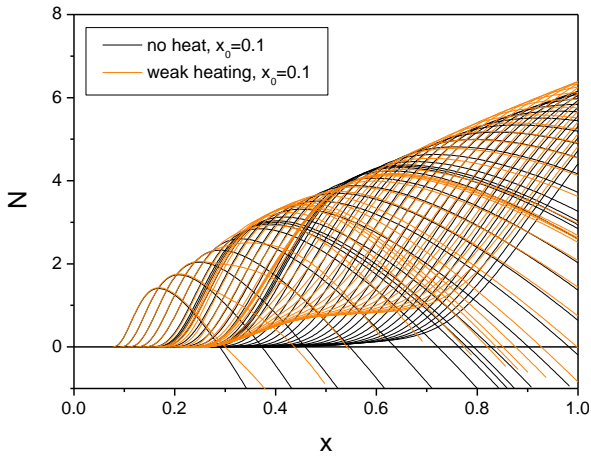


Fig. 14. N-factors for the weak heating case (orange lines) computed from the fixed point $x_0 = 0.1$ in comparison with baseline case (black lines).

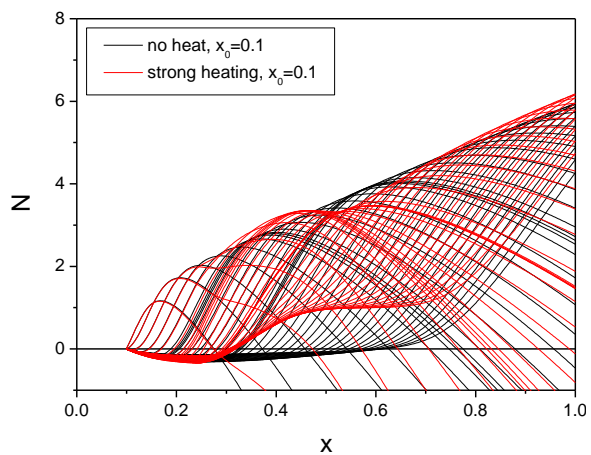


Fig. 15. N-factors for the strong heating case (red lines) computed from the fixed point $x_0 = 0.1$ in comparison with baseline case (black lines).

5 Direct numerical simulation

Direct numerical simulations are performed for the baseline case, the strong cooling case and the strong heating case. First, a steady-state solution, which satisfies the free-stream boundary conditions on the inflow and upper boundaries, is calculated to provide the mean flow on fine mesh. The computational grid has 6397×449 nodes. Then, time-harmonic disturbances are induced by a local periodic suction-blowing with the mass flow rate on the cone surface

$$q_w(x, t) = (\rho_w^* v_w^*) / (\rho_\infty^* U_\infty^*) = \varepsilon \sin(2\pi(x - x_1) / (x_2 - x_1)) \sin(\omega t), x_1 \leq x \leq x_2$$

where $\varepsilon = 1 \times 10^{-4}$ is forcing amplitude; $x_1 = 0.1$, $x_2 = 0.114$ are boundaries of the suction-blowing region. The circular frequency is $\omega = \omega^* L^* / U_\infty^* = 700$. The suction-blowing amplitude ε was chosen small enough to compare numerical results with LST. In the unsteady problem, the temperature disturbances on the wall are zero.

The local blowing-suction excites unstable disturbances in the boundary layer reaching its maximum near the end of computational domain. The pressure disturbance field, which is the difference between an instantaneous field and the mean-flow field) is shown in Figure 16 for the baseline case. For $x > 0.6$ the downstream growing disturbance is observed in the boundary layer.

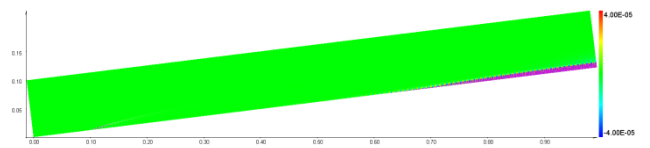


Fig. 16. Pressure disturbance field for the baseline case.

Detailed view of this instability in the region $0.85 \leq x \leq 0.95$ is shown in Figure 17 for the baseline case and the strong heating/cooling cases. The pressure disturbances have a two-cell structure in vertical direction. These patterns are typical for the Mack second mode [3]. Maximal amplitudes are observed in the strong-heating case, while the minimal amplitudes correspond to the strong-cooling case.

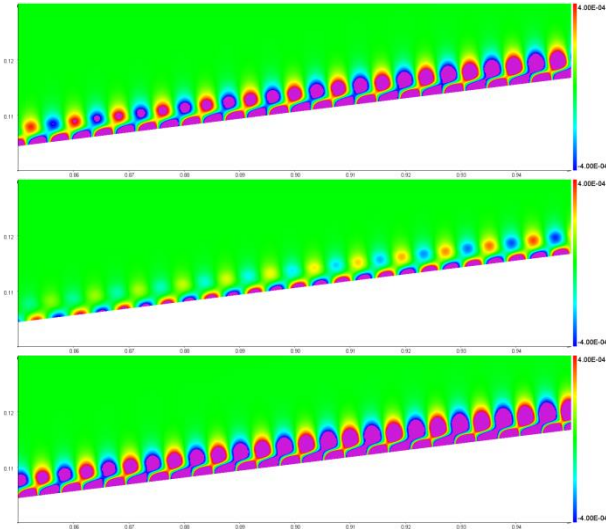


Fig. 17. Pressure disturbance field, $0.85 \leq x \leq 0.95$; upper – baseline, middle – strong cooling, lower – strong heating.

Figure 18 shows details of the wall pressure distributions $p'_w(x)$ in the vicinity of heating/cooling strip. The strip boundaries x_{S1} and x_{S2} are marked by the vertical red lines. In the upstream region $x < x_{S1}$, there is no noticeable difference between $p'_w(x)$ for the all three cases. In the strip region $x_{S1} < x < x_{S2}$, the disturbance amplitude decreases on the cold strip, while it increases on the hot strip. Further downstream ($x > x_{S2}$), the disturbance starts to grow with appreciable rate in the heating case and with weaker rate in the baseline case. For the cooling case, the disturbance amplitude decreases weakly.

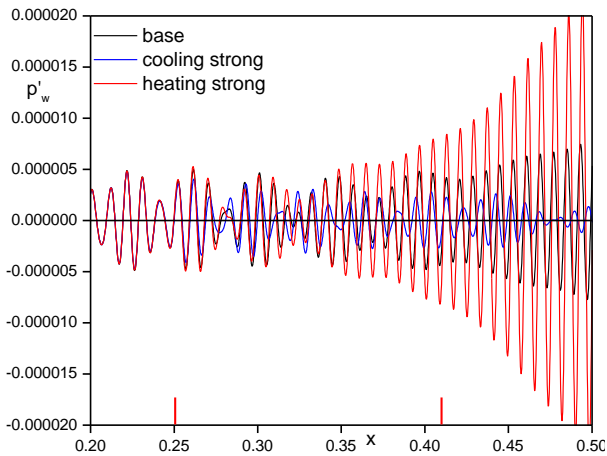


Fig. 18. Wall-pressure disturbances near the cooling/heating strip, $0.2 \leq x \leq 0.5$, $\omega = 700$; black curve – baseline, blue – strong cooling, red – strong heating.

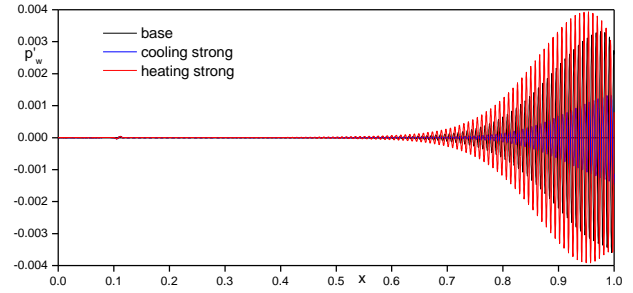


Fig. 19. Wall pressure disturbances, $\omega = 700$; black curve – baseline, blue – strong cooling, red – strong heating.

The global distributions of $p'_w(x)$ are shown in figure 19. The maximal wall-pressure disturbances are reached in the case of strong heating, while the minimal – in the case of strong cooling. This trend is the same as in experiments (Figure 6-7) and linear stability analysis (Figures 12 and 15).

6 Comparison of DNS and LST results

Additional LST computations were performed for the second-mode wave with the frequency being equal to the suction-blowing frequency of DNS ($\omega = 700$). Figure 20 shows comparisons of LST predictions with the DNS solutions. Since the LST analysis does not account for receptivity, the initial amplitudes of LST solutions are arbitrary. In this figure the amplitude ratio is scaled by a factor providing the best fit for the baseline case (black lines). The same factor is used for scaling in the two other cases. The agreement between DNS and LST solutions is satisfactory accounting for the fact that the LST analysis ignores the nonparallel effects, which are expected to be strong in the heating/cooling region.

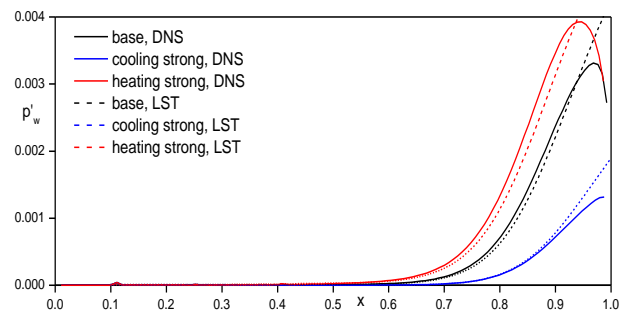


Fig. 20. Amplitudes of wall pressure disturbances, $\omega = 700$; black curve – baseline, blue – strong cooling, red – strong heating; computations from $x_0 = 0.1$.

6 Summary

A localized heating or cooling effect on stability of the boundary-layer flow on a sharp cone at zero angle of attack is analyzed at the free-stream Mach number 6. Five different temperature distributions were numerically simulated: baseline flow without heating or cooling, strong and weak cooling, strong and weak heating. The free-stream and surface conditions correspond to the experiments performed in the ITAM Transit-M wind tunnel (Novosibirsk).

DNS was performed for 2D disturbance excited by the suction-blowing slot located upstream from the strip. It was shown that the second mode instability is a dominant component of the disturbance field in the boundary layer downstream from the strip. It was found that the hot strip leads to relatively small increasing of the instability amplitude, while the cold strip produces an opposite effect.

The LST computations of the disturbances amplification starting from the suction-blowing locus are carried out. The mean flows are calculated using axisymmetric Navier-Stokes equations. The spatial LST analysis is performed for 2D disturbances related to the Mack second mode. LST results agree satisfactory with the DNS solutions.

The experiments and computations showed similar qualitative trends. The cooling strip decreases the second-mode amplitude and delays transition. The heating strip produced an opposite effect which is less pronounced.

This work was supported by TransHyBerIAN Project of the 7th Framework Program and partially by Russian Scientific Foundation under Grant 14-19-00821 and by the Mega-grant of the Russian Federation Government to support scientific research under the supervision of leading scientist at Novosibirsk State University, No. 14.Z50.31.0019.

References

[1] Kazakov AV, Kogan MN, and Kuparev VA. On the enhancement of the stability of a subsonic boundary layer by heating the surface near the leading edge of

the body. *Doklady Akad Nauk SSSR*, Vol. 3, pp. 333, 1985.

[2] Dovgal AV, Levchenko VY, and Timofeev VA. *Laminar-Turbulent Transition* (Ed. by D. Arnal and R. Miche), Springer-Verlag, Berlin, 1990.

[3] Egorov IV, Fedorov AV, and Soudakov VG. Direct numerical simulation of disturbances generated by periodic suction-blowing in a hypersonic boundary layer. *Theoret. Comput. Fluid Dynamics*, Vol. 20, No 1, pp. 41-54, 2006.

7 Contact Author Email Address

vit_soudakov@tsagi.ru

Copyright Statement

The authors confirm that they, and/or their company or organization, hold copyright on all of the original material included in this paper. The authors also confirm that they have obtained permission, from the copyright holder of any third party material included in this paper, to publish it as part of their paper. The authors confirm that they give permission, or have obtained permission from the copyright holder of this paper, for the publication and distribution of this paper as part of the ICAS 2014 proceedings or as individual off-prints from the proceedings.